

Ab initio study of orbital-selective superconductivity in γ -BiPd

Sonu Prasad Keshri¹ and Guang-Yu Guo^{1,2,*}

¹*Department of Physics, National Taiwan University, Taipei 10617, Taiwan*

²*Physics Division, National Center for Theoretical Sciences, Taipei 10617, Taiwan*

(Dated: November 27, 2025)

We investigate the superconducting (SC) properties of experimentally realised γ -BiPd by solving the anisotropic Migdal-Eliashberg equations in conjunction with *ab initio* relativistic calculations of the electron and phonon band structures as well as electron-phonon coupling (EPC) matrix elements. Our study reveals that γ -BiPd possesses a complex Fermi surface (FS), consisting of two electron pockets and one hole pocket, each characterised by distinct atomic orbitals. Our key finding is that the superconductivity in γ -BiPd is primarily orbital-selective, arising from Bi *p*-orbitals, and distributed anisotropically on the FS, although contribution from Pd *d*-orbitals, particularly on the hole pocket, is also discernable. While our results show an anisotropic nature of the \mathbf{k} -dependent SC gap $\Delta_{\mathbf{k}}$ and EPC strength $\lambda_{\mathbf{k}}$ across the FS, calculated superconducting quasiparticle density of states N_S spectra exhibit a U-shaped gap and $\Delta_{\mathbf{k}}$ distribution forms a single peak, being consistent with the spin-singlet *s*-wave superconductivity observed in this material. The calculated T_c is ~ 2.0 K, agreeing in order of magnitude with the experimental value of 3.3 K in γ -BiPd thin films. The predicted EPC-enhanced Sommerfeld coefficient γ_n of $0.141 \text{ mJ/K}^2\text{cm}^3$ is similar to the experimental γ_n value ($0.119 \text{ mJ/K}^2\text{cm}^3$) of the isoelectronic and isostructural Bi(Pd_{0.5}Pt_{0.5}) alloy.

I. INTRODUCTION

The discovery of strong \mathbf{k} -dependent and multigap superconductivity, which was observed experimentally as early as 1980 [1] and extensively studied theoretically [2] since the advent of the Bardeen–Cooper–Schrieffer (BCS) theory [3], has provided new physical insights. These include chiral ground states [4], vortices with fractional flux [5], and topological solitons [6]. Anisotropic and multigap superconductivity can be introduced by the combined effects of the normal state quantities N_F , V , and ω_c [1], which enter in the superconducting (SC) gap Δ in the weak-coupling isotropic BCS limit as $\Delta = 2\hbar\omega_c e^{[-2/N_F V]}$, where N_F is the density of states (DOS) near the Fermi level (E_F), V the electron-phonon coupling (EPC) potential, and ω_c the cutoff phonon angular frequency [3, 7]. Another significant quantity from the normal state is the Fermi velocity (v_f), which plays a role in the current density for penetration phenomena.

In systems with multiple bands crossing the E_F , each band can contribute differently to N_F and V , depending on the correlation strength of each band or orbital [2]. Binary compound MgB₂ has been shown multiband (σ and π bands) superconductivity with transition temperature $T_c \sim 39$ K where EPC is the sole source of pairing [8–12]. Subsequently many Fe-based superconductors such as FeSe [13–17], LaFeAsO_{1-x}F_x-based superconductors [18–22], and many others including NbS₂ [23–25], NbSe₂ [26], and TiTe₂ [27] have been shown multiple electron and hole pockets. In FeSe, Fe d_{xz} , d_{yz} and d_{xy} orbitals dominate the bands near the E_F and thus would lead to the orbital-selective superconductivity. The interplay of signs of electron and hole pockets on the Fermi

surface (FS) has led to the classification of *s*-wave superconductors as s_{\pm} and s_{++} waves [18, 28].

Bi-Pd-based alloys have recently attracted significant interest in the scientific community due to their potential for topological superconductivity and the discovery of various pairing mechanisms [29–37]. These alloys exist in multiple allotropes and phases [36, 38]. Among them, α -BiPd, β -Bi₂Pd and γ -BiPd were recently found to show T_c of 3.7, 3.6, and 3.3 K, respectively [36]. Tetragonal β -Bi₂Pd (I₄/mmm) and hexagonal γ -BiPd (P6₃/mmc) are centrosymmetric, and were reported to show triplet pairing and singlet pairing, respectively [36]. The centrosymmetric γ -BiPd would transform to noncentrosymmetric α -BiPd after post-annealing at 270^o C. Thus, monoclinic α -BiPd (P2₁) [29] would exhibit an admixture of singlet and triplet pairing [36, 39] because of the lack of inversion symmetry combined with Rashba spin-orbit coupling (SOC) [39–41]. In α -BiPd, topological phenomena such as Dirac surface states have been observed, and the material has been investigated for topological superconductivity [32, 42]. The SOC would also introduce exotic proximity effects at superconductor/ferromagnet (S/F) interface [43–48]. In this context, SOC acts as an exchange interaction, converting spin-singlet pairing into spin-triplet pairing. It also gives rise to a new class of superconductors known as type I and type II Ising superconductors [49–52].

Despite the different crystal structures and pairing mechanisms, the three Bi-Pd alloys have almost the same T_c . Similar to α -BiPd, β -Bi₂Pd is also topologically nontrivial, and its SC properties are extensively studied in the quest for novel phenomena such as Andreev bound states and Majorana fermions [30, 31, 33, 34, 36]. The upper critical magnetic field and specific heat measurements initially suggested that β -Bi₂Pd could be a multigap superconductor [30]. However, subsequent investigations using scanning tunneling microscopy and muon-spin re-

* gyguo@phys.ntu.edu.tw

laxation experiments confirmed that β -Bi₂Pd is actually a single-gap BCS superconductor [34].

Among the three Bi-Pd alloys, γ -BiPd has received relatively little theoretical attention despite its nontrivial topology [36, 37]. γ -BiPd features a simple hexagonal crystal structure (Fig. 1) and exhibits spin-singlet s -wave superconductivity [36]. Yet, its T_c matches closely with those of α -BiPd and β -Bi₂Pd, which raises intriguing questions about the microscopic normal state features that lead to these distinct SC states. To explore these questions, we have investigated the SC properties of γ -BiPd by solving the anisotropic Migdal-Eliashberg equations and then evaluating \mathbf{k} -dependent SC gap $\Delta_{\mathbf{k}}$, T_c and SC quasiparticle DOS (N_s). Our primary finding is that the superconductivity in γ -BiPd is mainly orbital-selective and anisotropic. Our calculated T_c is ~ 2.0 K, being in reasonable agreement with the experimental value of ~ 3.3 K in γ -BiPd thin films [36]. The $\Delta_{\mathbf{k}}$ on the FS forms a single gap, although it is anisotropic, and the N_s spectra exhibit a U-shaped gap. All these findings are consistent with the spin-singlet s -wave superconductivity observed in γ -BiPd films [36].

The rest of this paper is arranged as follows. In Sec. II, we provide an overview of the *ab initio* Migdal-Eliashberg theory of superconductivity adopted in this study. This section also gives details of various intermediate quantities involved. In Sec. III, we provide the computational details of the *ab initio* calculations conducted in this study. In Sec. IV, we report the theoretical crystal structure and calculated phonon dispersion. In Sec. V, the electronic structure, FS, and the atomic orbital contributions on the FS are presented. In Sec. VI, we present the EPC strength as a function of phonon energy in the Brillouin zone (BZ), and examine its distribution on the FS. In Sec. VII, SC properties are presented, including the \mathbf{k} -dependent SC gap and its orbital characters, the T_c , and the N_s . We summarize the main results of this study in Sec. VIII. Finally, we show the significant SOC effect on the energy bands in the vicinity of the Fermi level in γ -BiPd in Appendix A, and also report the calculated Coulomb pseudopotential dependence of T_c and SC gap function in Appendix B.

II. METHODOLOGY

We calculate the \mathbf{k} -dependent SC gap, the T_c and SC quasiparticle DOS by solving the anisotropic Migdal-Eliashberg (ME) equations. A small energy window near the E_F defined by $\hbar\omega_{ph}$ is important, as the pair formation takes place in this energy window. In the vicinity of the FS, there are two anisotropic ME equations to solve, one for the renormalization function $Z(j\mathbf{k}, i\omega_n)$ and the other for the order parameter $\phi(j\mathbf{k}, i\omega_n) =$

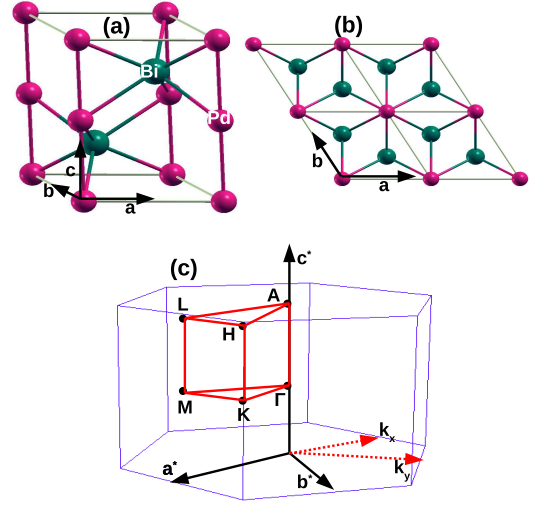


FIG. 1. (a) A side-view and (b) the z -axis view of crystal structure of γ -BiPd. In (b), the $2 \times 2 \times 1$ supercell is shown. The associated BZ is illustrated in (c).

$Z(j\mathbf{k}, i\omega_n)\Delta(j\mathbf{k}, i\omega_n)$ given by [53]

$$Z(j\mathbf{k}, i\omega_n) = 1 + \frac{\pi T}{\omega_n} \sum_{j'\mathbf{k}'n'} W_{j'\mathbf{k}'} \frac{\omega_n}{\sqrt{R(j'\mathbf{k}', i\omega_{n'})}} \times \lambda(j\mathbf{k}, j'\mathbf{k}', n - n'), \quad (1)$$

and

$$Z(j\mathbf{k}, i\omega_n)\Delta(j\mathbf{k}, i\omega_n) = \pi T \sum_{j'\mathbf{k}'n'} W_{j'\mathbf{k}'} \frac{\Delta(j'\mathbf{k}', i\omega_{n'})}{\sqrt{R(j'\mathbf{k}', i\omega_{n'})}} \times \left[\lambda(j\mathbf{k}, j'\mathbf{k}', n - n') - N_F V(j\mathbf{k} - j'\mathbf{k}') \right], \quad (2)$$

with $R(j\mathbf{k}, i\omega_n) = \omega_n^2 + \Delta^2(j\mathbf{k}, i\omega_n)$ and $W_{j\mathbf{k}} = \delta(\epsilon_{j\mathbf{k}})/N_F$, where $i\omega_n = i(2n + 1)\pi T$ is fermion Matsubara frequencies, n is an integer and T is the absolute temperature. We set $\hbar = k_B = 1$. $V(j\mathbf{k} - j'\mathbf{k}')$ is the matrix elements of the static screened Coulomb interaction between the electronic states $j\mathbf{k}$ and $j'\mathbf{k}'$, and $\lambda(j\mathbf{k}, j'\mathbf{k}', n - n')$ is the anisotropic EPC parameter given by

$$\lambda(j\mathbf{k}, j'\mathbf{k}', n - n') = \int_0^\infty d\omega \frac{2\omega}{(\omega_n - \omega_{n'})^2 + \omega^2} \times \alpha^2 F(j\mathbf{k}, j'\mathbf{k}', \omega). \quad (3)$$

The quantity $\alpha^2 F(j\mathbf{k}, j'\mathbf{k}', \omega)$ is the anisotropic Eliashberg spectral function expressed as

$$\alpha^2 F(j\mathbf{k}, j'\mathbf{k}', \omega) = N_F \sum_{\nu} |g_{jj'\mathbf{k}\mathbf{k}'\nu}|^2 \delta(\omega - \omega_{j\mathbf{k}-j'\mathbf{k}',\nu}). \quad (4)$$

The electron-phonon matrix elements $g_{jj'\mathbf{k}\mathbf{k}'\nu}$ are expressed in terms of derivatives of the self-consistent potential $\partial_{\mathbf{q}\nu}V_{sc}$ as $g_{jj'\mathbf{k}\mathbf{k}'\nu} = \langle \psi_{j'\mathbf{k}'} | \partial_{\mathbf{q}\nu}V_{sc} | \psi_{j\mathbf{k}} \rangle$, associated with a phonon of wave vector \mathbf{q} and branch ν . $\psi_{j\mathbf{k}}$ is the electronic wavefunction for wavevector \mathbf{k} in band j . The electronic eigen energies $\epsilon_{j\mathbf{k}}$ are taken near the E_F . In the present calculations, the \mathbf{k} - and \mathbf{q} -meshes are chosen to be uniform and they satisfy the condition $\mathbf{q} = \mathbf{k}' - \mathbf{k}$ and must be commensurate.

The phonon-mode resolved EPC $\lambda_{\mathbf{q}\nu}$ is given by

$$\lambda_{\mathbf{q}\nu} = \frac{1}{N_F \omega_{\mathbf{q}\nu}} \sum_{j\mathbf{k}, j'\mathbf{k}'} W_{j\mathbf{k}} |g_{jj'\mathbf{k}\mathbf{k}'\nu}|^2 \delta(\epsilon_{j\mathbf{k}}) \delta(\epsilon_{j'\mathbf{k}'}), \quad (5)$$

where δ is the Dirac delta function.

The SC quasiparticle DOS relative to the normal-state DOS at the E_F is

$$\frac{N_s(\omega)}{N_F} = \sum_j \int_{BZ} \frac{d\mathbf{k}}{\Omega_{BZ}} \frac{\delta(\epsilon_{j\mathbf{k}} - \epsilon_F)}{N_F} \text{Re} \left[\frac{\omega}{\sqrt{\omega^2 - \Delta_{j\mathbf{k}}^2(\omega)}} \right], \quad (6)$$

where Ω_{BZ} is the BZ volume, and $\Delta_{j\mathbf{k}}$ is the complex energy-dependent gap for band j and momentum \mathbf{k} .

III. COMPUTATIONAL DETAILS

The QUANTUM ESPRESSO package [54, 55] is adopted here for the structural optimization, electronic structure, and phonon dispersion calculations in a fully first-principles way. Because γ -BiPd contains heavy Bi atoms, the presence of relativistic SOC would significantly modify the electronic band structure of γ -BiPd, especially the energy bands near the E_F , as demonstrated in Appendix A. Therefore, all the results presented in this paper are obtained from the first-principles calculations with the SOC included. The Perdew-Burke-Ernzerhof solid (PBEsol) type exchange-correlation functional along with the optimized norm-conserving Vanderbilt relativistic pseudopotentials [56] are used. The kinetic-energy cutoff of 100 Ry, and the Methfessel-Paxton smearing width of 0.02 Ry is used. The self-consistent field (SCF) charge density is computed on the Γ -centered \mathbf{k} -mesh of $12 \times 12 \times 8$. For the DOS and FS calculations, a dense \mathbf{k} -mesh of $36 \times 36 \times 18$ is used. The phonon dispersion and linear variation of the self-consistent potential were calculated using density functional perturbation theory (DFPT) [57] on the $6 \times 6 \times 3$ \mathbf{q} -mesh with threshold for self-consistency of 10^{-14} . We use the EPW code to calculate the SC properties in the anisotropic ME formalism with the electron-phonon interpolation in Wannier manifold [53, 58–60]. Solutions of the ME equations are sensitive to the sampling of electron-phonon matrix elements near the E_F . To obtain converged results, it requires a dense \mathbf{k} and \mathbf{q} -point

meshes. These shortcomings are overcome by employing interpolation method based on first-principles calculations in conjunction with maximally localized Wannier functions [53] as implemented in the EPW code. The band structure calculation required for the Wannier interpolation is done on uniform \mathbf{k} -point mesh of $12 \times 12 \times 6$. The ME equations are solved by calculating the electron-phonon matrix elements in the proximity of the Fermi energy on fine grids of \mathbf{k} -points and \mathbf{q} -points of $64 \times 64 \times 32$ and $32 \times 32 \times 16$, respectively. The Fermi window used is 0.4 eV. We also examine the convergence of the gap function and anisotropic EPC strength with respect to both fine \mathbf{k} - and \mathbf{q} -mesh samplings, ensuring that the final result is well-converged.

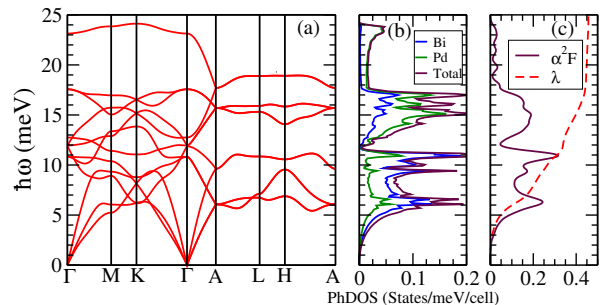


FIG. 2. (a) Phonon dispersion, (b) phonon DOS (PhDOS), (c) Eliashberg spectral function ($\alpha^2 F$), and accumulative electron-phonon coupling constant ($\lambda(\omega)$) of γ -BiPd.

IV. CRYSTAL STRUCTURE AND PHONON DISPERSION

The unit cell of γ -BiPd contains two formula units (two Bi and two Pd atoms per unit cell) organised in a hexagonal structure with space group $P6_3/mmc$ (No. 194) (Fig. 1). In the present calculations, the fully optimised lattice constants $a = 4.2719 \text{ \AA}$ and $c = 5.6244 \text{ \AA}$ are used, which agree well with the experimental lattice parameters of $a = 4.23 \text{ \AA}$ and $c = 5.69 \text{ \AA}$ [61] (with errors within $\sim 1\%$). The Wyckoff positions of Pd atoms and Bi atoms are $2a (0, 0, 0)$ and $2c (1/3, 2/3, 1/4)$, respectively (Fig. 1). Each Bi atom is coordinated by six Pd atoms, while each Pd atom is bonded to six Bi atoms and two additional Pd atoms. The Bi-Pd bond length is 2.8391 \AA , while the Pd-Pd bond length is slightly shorter at 2.8122 \AA . The nearest Bi-Bi separation is 3.7406 \AA . The Pd-Bi-Pd bond angle is 59.375° , and the Bi-Pd-Pd bond angle is 60.312° .

The calculated phonon dispersion and phonon DOS are presented in Figs. 2(a) and 2(b), respectively. The phonon spectrum of γ -BiPd includes 12 modes: three acoustic and nine optical ones, as shown in Fig. 2(a). Below 12.3 meV, the phonon DOS is dominated by Bi-atomic vibrations, attributed to the heavier mass of Bi atoms. Above this energy, Pd atomic vibrations become

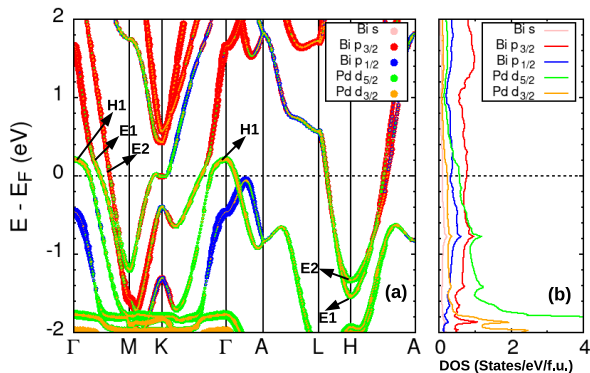


FIG. 3. (a) Orbital-projected fat plot of the band structure, with the orbital weights being proportional to the sizes of the corresponding colored dots and (b) orbital-projected DOSs of γ -BiPd. In (a), one band labelled H1 represents the hole pocket, and two bands labelled E1 and E2 form the two electron pockets.

increasingly dominant. The Γ -point in the Brillouin zone (BZ) exhibits centrosymmetric point group symmetry $D_{6h}(6/mmm)$. Within this symmetry, the longitudinal acoustic phonon mode corresponds to the A_{2u} representation, while the two transverse acoustic modes belong to the E_{1u} representation. In the acoustic region, the transverse modes exhibit higher frequencies than the longitudinal mode. In contrast, in the optical region, the longitudinal optical modes have higher frequencies than the transverse optical modes.

V. ELECTRONIC STRUCTURE AND FERMI SURFACE

In Fig. 3(a) and Fig. A1, we show fully relativistic electronic band structure of γ -BiPd, and in Fig. 3(a), the sizes of Bi and Pd orbital contributions are indicated by the sizes of color dots. In Fig. 3(b), Bi and Pd orbital-projected DOS spectra are displayed. In the presence of the SOC, atomic orbitals of orbital angular momentum l would split into two sets of sub-orbitals with total angular momentum $j = l - s$ and $j + s$, respectively. Here $s = 1/2$ is the spin angular momentum. In particular, p -orbitals would split into doubly degenerate $p_{1/2}$ -orbitals of $j = 1/2$ and four-fold degenerate $p_{3/2}$ -orbitals of $j = 3/2$. And d -orbitals would split into four-fold degenerate $d_{3/2}$ -orbitals of $j = 3/2$ and six-fold degenerate $d_{5/2}$ -orbitals of $j = 5/2$. In the vicinity of the Fermi level, the DOS is mainly of Bi p -orbital and Pd d -orbital characters [Fig. 3(b)]. For example, Bi $p_{3/2}$ -orbitals dominates the DOS near the E_F , while the second largest contribution comes from Pd $d_{5/2}$ -orbitals. Specifically, total DOS at the E_F $N_F = 1.10$ states/eV/BiPd, and atom-decomposed DOSs at the E_F are 0.644 and 0.416 states/eV/atom, respectively, for Bi and Pd atoms. Orbital-projected DOSs at the E_F

for Bi s , $p_{1/2}$ and $p_{3/2}$ as well as Pd $d_{3/2}$ and $d_{5/2}$ are, respectively, 0.054, 0.180, 0.409, 0.119 and 0.294 states/eV/atom. Interestingly, Fig. 3(b) indicates that all the orbital-projected DOS spectra are rather flat in the vicinity of the E_F and are almost constant over a narrow energy window of 0.1 eV around the Fermi level.

Figures 3(a) and A1 show that three bands [labelled H1, E1 and E2 in Fig. 3(a)] cross the E_F , indicating metallic behavior of γ -BiPd. As a result, the Fermi surface consists of three Fermi sheets (pockets), as shown in Fig. 4. The H1 band forms a hole pocket centered at the Γ point, while the E1 and E2 bands form two large electron-like Fermi sheets. Analyzing the orbital contributions near the high-symmetry points [Fig. 3(a)], we find that the H1 band near the E_F at the Γ -point arises primarily from Pd d -orbitals. Their relatively localized nature results in a low Fermi velocity v_f [Fig. 4(a)]. On the other hand, the E1 and E2 electron pockets span a large portion of the BZ [Figs. 4(b) and (c)], and thus contribute more significantly to the DOS near the E_F . These bands are highly dispersive and anisotropic, leading to larger and direction-dependent Fermi velocities. For instance, the E2 band at the K point near the E_F exhibits strong hybridization between Pd $d_{3/2}$ - and $d_{5/2}$ -orbitals and Bi $p_{3/2}$ -orbitals. It forms an open neck at the K-point with a relatively low v_f , while along the Γ -A direction, its dispersive character results in a high v_f .

VI. ELECTRON-PHONON COUPLING

For phonon-mediated superconductors, the ME theory has proven effective in predicting both the T_c and the anisotropic SC gap [23, 53]. Two main ingredients, namely, Eliashberg spectral function α^2F and effective Coulomb repulsion potential μ_c^* , are required to solve the ME equations [Eqs. (1) and (2)] [53]. The effective Coulomb repulsion enters the formalism via the momentum-dependent Coulomb matrix elements $V(\mathbf{k} - \mathbf{k}')$ [Eq. (2)] [59]. The Coulomb potential is double-averaged over the FS, yielding an effective Coulomb interaction $\mu_c = N_F \langle \langle V(\mathbf{k} - \mathbf{k}') \rangle \rangle_{\text{FS}}$. In the ME equations, this averaged interaction replaces the term $N_F V(\mathbf{k} - \mathbf{k}')$ with its renormalized form μ_c^* , called Morel-Anderson pseudopotential. This Coulomb pseudopotential μ_c^* has often been treated as a semiempirical parameter [58–60], and the μ_c^* value of ~ 0.10 has been widely used for conventional superconductors especially classic elemental superconductors [62]. It has also been found that $\mu_c^* \approx 0.05 \sim 0.10$ works quite well for many sp -electron systems, while $\mu_c^* \approx 0.10 \sim 0.15$ is quite appropriate for transition metal compounds [62].

The Eliashberg spectral function α^2F , shown in Fig. 2(c), represents the frequency-resolved EPC. The shape of α^2F closely follows the phonon DOS, consisting of three distinct peaks: one corresponding to the acoustic phonons and two arising from the optical phonons. The phonon DOS spectrum can be divided into two re-

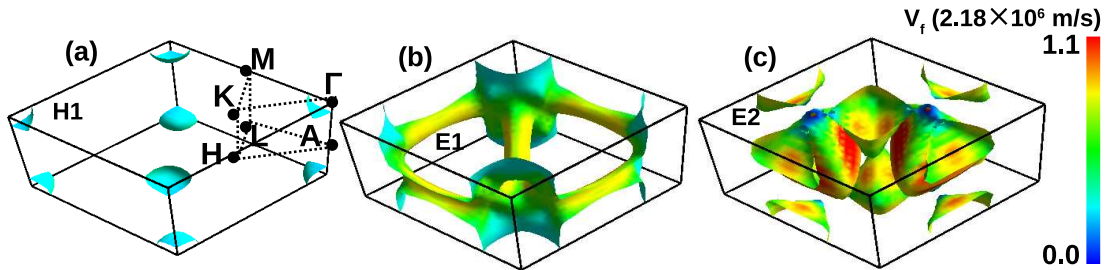


FIG. 4. Momentum \mathbf{k} -dependent magnitude of the Fermi velocity v_f on the Fermi surface of γ -BiPd on (a) hole pocket H1, (b) electron pocket E1, and (c) electron pocket E2.

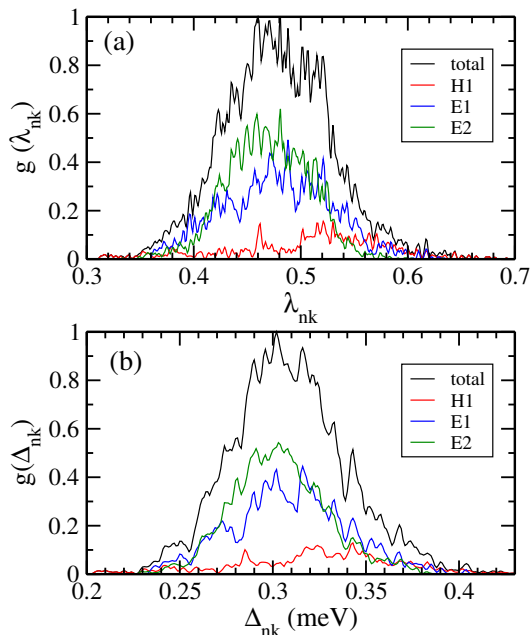


FIG. 5. Total and band-resolved normalized density distribution of (a) the EPC strength $\lambda_{n\mathbf{k}}$, $g(\lambda_{n\mathbf{k}})$, and of (b) SC gap $\Delta_{n\mathbf{k}}$, $g(\Delta_{n\mathbf{k}})$, on the FS of γ -BiPd.

gions at energy of 12.3 meV. This separation originates from the significant mass difference between Bi and Pd atoms. This separation is followed up in α^2F , reflecting the atomic character of EPC across the frequency spectrum. Specifically, the portion of α^2F below 12.3 meV, including two prominent peaks, is primarily attributed to Bi-related vibrational modes. In contrast, the broader peak above 12.3 meV is predominantly governed by the vibrations of lighter Pd atoms.

The total EPC constant λ , also known as the mass enhancement parameter, is obtained by integrating α^2F/ω over the entire frequency range. The calculated EPC constant λ of γ -BiPd is 0.46, and this places γ -BiPd among the intermediate strong-coupled superconductors such as Al and Ga [63]. From the cumulative λ shown in Fig. 2 (c), we observe that approximately 80% of the

total λ arises from Bi-atomic vibrations occurring below 12.3 meV. The remaining contribution comes from Pd-atomic vibrations. This clearly highlights the dominant role of Bi atoms in the EPC, particularly within the acoustic phonon region. Since the phonon DOS spectrum of γ -BiPd could be roughly separated into the Bi vibration dominant low frequency region and the Pd oscillation dominant high frequency region at 12.3 meV [(Fig. 2(b)), the EPC strength λ could be broken down into contributions from the electronic stiffness $K_{e,j}$ and the lattice stiffness $K_{l,j}$ of the two atoms (j denotes either Bi or Pd), expressed as $\lambda_j = \frac{K_{e,j}}{K_{l,j}}$ [7]. The $K_{e,j}$ and $K_{l,j}$ are known to be proportional to the atom-decomposed DOS at the E_F and the second moment of phonon frequency, respectively [7]. As discussed above, in γ -BiPd, Bi atom would have a larger DOS at the E_F than Pd atom, and would have a lower second moment of phonon frequency than Pd. Consequently, Bi atom would have a higher K_e and a lower K_l than Pd atom, thus resulting in a larger contribution to the EPC constant λ than Pd atom.

In Fig. 5(a), we present the normalized distribution of total and band-decomposed EPC strength $\lambda_{\mathbf{k}}$ on the FS. This quantity represents the probability density of the electron-phonon interaction over the FS. The distribution is centered around $\lambda_{\mathbf{k}} = 0.46$ with a rather broad width, indicating significant anisotropy in the EPC on the FS. Figure 5(a) indicates that bands E1 and E2 make dominant contributions to the EPC.

Figures 6 show momentum-resolved $\lambda_{\mathbf{k}}$ on the three Fermi sheets. The $\lambda_{\mathbf{k}}$ would contribute to the renormalization of both the energy bands and the DOS at the E_F , quantified by the renormalization function $Z_{\mathbf{k}} = 1 + \lambda_{\mathbf{k}}$. Fermi velocity $v_{\mathbf{k}}$ would be reduced by a factor of $Z_{\mathbf{k}}$, while the DOS and related quantities such as electronic specific heat would be enhanced by the same factor. In the parabolic approximation, the effective mass m^* is related with $v_{\mathbf{k}}$ as $m^* = \hbar k_F/v_{\mathbf{k}}$, leading to an enhancement of $Z_{\mathbf{k}}$. These renormalizations due to the EPC can be measured in thermodynamic experiments such as specific heat and thermal conductivity. For example, the electronic contribution to the specific heat of a free-electron metal in the low temperature limit is given

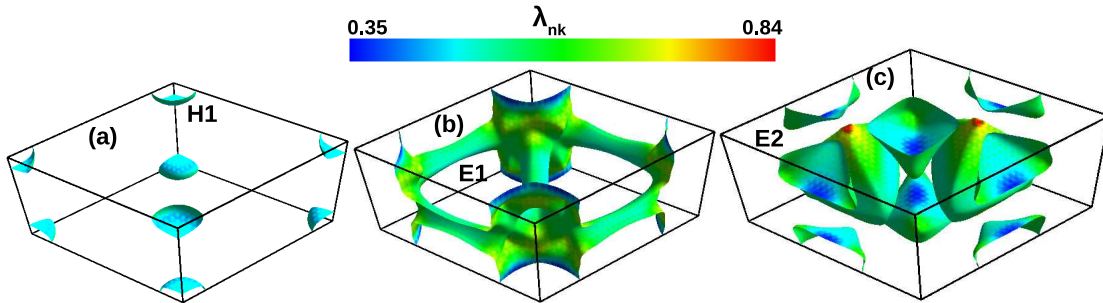


FIG. 6. Momentum \mathbf{k} -dependent EPC strength $\lambda_{\mathbf{k}}$ on the Fermi surface of γ -BiPd on (a) hole pocket H1, (b) electron pocket E1, and (c) electron pocket E2.

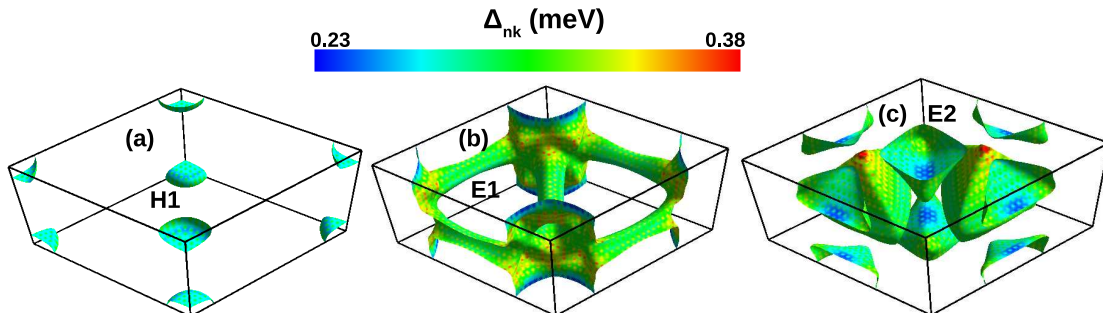


FIG. 7. Momentum \mathbf{k} -dependent SC gap $\Delta_{n\mathbf{k}}$ on the Fermi surface of γ -BiPd at 0.5 K on (a) hole pocket H1, (b) electron pocket E1, and (c) electron pocket E2.

by $C_e = \gamma_n T$ where normal state Sommerfeld coefficient $\gamma_n = \frac{\pi^2}{3} k_B^2 N_F$. In the presence of the EPC, γ_n would be enhanced by a factor of $(1.0 + \lambda)$ because N_F would be increased by the same factor. For γ -BiPd, $N_F = 1.10$ states/eV/BiPd and $\lambda = 0.46$. Therefore, the γ_n would be 0.097 mJ/K²cm³ and 0.141 mJ/K²cm³, respectively, before and after considering the EPC enhancement. The experimental γ_n value has not been reported for γ -BiPd. Nevertheless, specific heat experiments were recently performed on the Bi(Pd_{0.5}Pt_{0.5}) alloy, which is both isoelectronic and isostructural to γ -BiPd [37]. The measured γ_n for Bi(Pd_{0.5}Pt_{0.5}) is 0.119 mJ/K²cm³, which is close to our predicted EPC-enhanced γ_n value.

VII. SUPERCONDUCTING PROPERTIES

To obtain the SC gap function $\Delta_{n\mathbf{k}}$, we solve the anisotropic ME equations at several temperatures using $\mu_c^* = 0.05$ [62, 64], which is adopted here mainly because the DOS near the E_F is dominated by Bi p -orbitals (see Fig. 3). The influence of the choice of μ_c^* on the calculated SC gap function and T_c is discussed in Appendix B (Also see, e.g., Refs. [62] and [64]). In Fig. 5(b), we display the normalized distribution of total and band-decomposed SC gap $\Delta_{n\mathbf{k}}$ calculated at 0.6 K. The distribution is clustered around $\Delta_{\mathbf{k}} = 0.31$ meV

with a rather broad width of 0.15 meV, suggesting significant anisotropy in the SC gap on the FS. Figure 7 shows momentum-resolved SC gap $\Delta_{n\mathbf{k}}$ at 0.5 K on the FS, and indicates that the gap opening occurs on all three Fermi sheets. The $\Delta_{n\mathbf{k}}$ exhibits pronounced anisotropy across the FS. Electron Fermi sheet E2 exhibits the largest anisotropy [Fig. 7(c)], while hole pocket H1 displays the least anisotropy [Fig. 7(a)]. The calculated lowest and highest gap magnitudes are 0.23 meV and 0.38 meV, respectively, located on the E2 Fermi sheet. In particular, the largest SC gap is located near the K-point on a narrow neck of the E2 Fermi sheet [Fig. 7(c)].

Figure 5(b) shows that γ -BiPd is a single-gapped anisotropic superconductor, although the $\Delta_{n\mathbf{k}}$ varies across the FS (Figure 7), as mentioned above. This is consistent with the spin-singlet s -wave superconductivity observed in recent quantum oscillation measurements on γ -BiPd films [36]. Interestingly, recent experiments (see, e.g., [34, 65]) indicated that β -Bi₂Pd also has a single s -wave superconducting gap, although earlier experiments [30] suggested it to be a multigap superconductor based on the anomalous temperature dependences of the upper critical magnetic field and specific heat measurements. From Fig. 5, Fig. 6 and Fig. 7, a clear correspondence between $\lambda_{\mathbf{k}}$ and $\Delta_{n\mathbf{k}}$ is evident. This could be expected because γ -BiPd is predominantly a phonon-mediated superconductor. This behavior has been also

observed in other conventional superconductors such as NbS₂ [23] and PbTaSe₂ [66].

The anisotropy in the gap function of γ -BiPd can be further understood from the orbital characterization of the energy bands near the Fermi level [Fig. 3(a)]. The SC gap on the H1 Fermi sheet primarily originates from Pd d -orbitals. In contrast, the E1 and E2 Fermi sheets exhibit predominant Bi p -orbital characters. Since the E1 and E2 Fermi sheets span a large portion of the BZ and dominate the DOS near the E_F , the SC gap in γ -BiPd is largely governed by Bi p -orbitals. This Bi dominance is further corroborated by the fact that the EPC strength is mainly derived from the acoustic and low-energy optical phonon modes, which are predominantly associated with Bi atomic vibrations [see Figs. 2(b) and 2(c)]. Nonetheless, the role of Pd d -orbitals, particularly Pd $d_{5/2}$ components, remains non-negligible, especially in shaping the SC properties of the H1 band. The K-point which exhibits the largest SC gap magnitude on the E2 Fermi sheet is contributed mainly from hybridization of Pd d and Bi $p_{3/2}$ -orbitals. These orbital-specific participations suggest that the superconductivity in γ -BiPd is inherently orbital-selective, with the pairing amplitude modulated by the orbital-projected DOS involved. This provides a microscopic basis for the anisotropic yet single-gap superconductivity found in the system.

Such orbital-selective behaviors have been found in other SC materials, including iron-based superconductors FeSe [13–17] and LaFeAsO_{1-x}F_x [18–22] as well as conventional superconductors MgB₂, NbSe₂ [26] and NbS₂ [23, 24]. In particular, three Fe d_{xz} , d_{yz} and d_{xy} orbitals dominate the electronic states near the E_F and thus give rise to the multiorbital superconductivity in FeSe. In LaFeAsO_{1-x}F_x, although there is significant hybridization among five Fe d -orbitals, which form four Fermi sheets, the SC gap retains the s -wave symmetry with opposite signs between electron and hole pockets. Similarly, in conventional superconductor 2H-NbS₂ [23], three Fermi sheets are present, and pairing contributions from S p_z and Nb d -orbitals exhibit different amplitudes. It leads to two distinct and \mathbf{k} -dependent SC gaps as measured experimentally [25] and latter explained theoretically [23]. The anisotropic and orbital dependent SC gap can be measured using quasiparticle interference imaging [25], high resolution angle-resolved photoemission spectroscopy (ARPES) [67, 68], and scanning tunneling microscopy and spectroscopy (STM and STS) [69].

In Fig. 8(a), the SC gap Δ calculated at several different temperatures are plotted. To evaluate the superconducting T_c , the averaged SC gap values at the considered temperatures [denoted by red dots in Fig. 8(a)] are fitted using a BCS-type temperature dependence [3]

$$\Delta(T) = \Delta(0)\tanh(\alpha\sqrt{T_c/T - 1}). \quad (7)$$

We obtain $\Delta(0) = 0.305$ meV, $\alpha = 1.90$ and $T_c = 1.96$ K. The calculated T_c of 1.96 K agree reasonably well with the experimental value of ~ 3.3 K reported for γ -BiPd thin films [36]. The obtained α of 1.90 is slightly

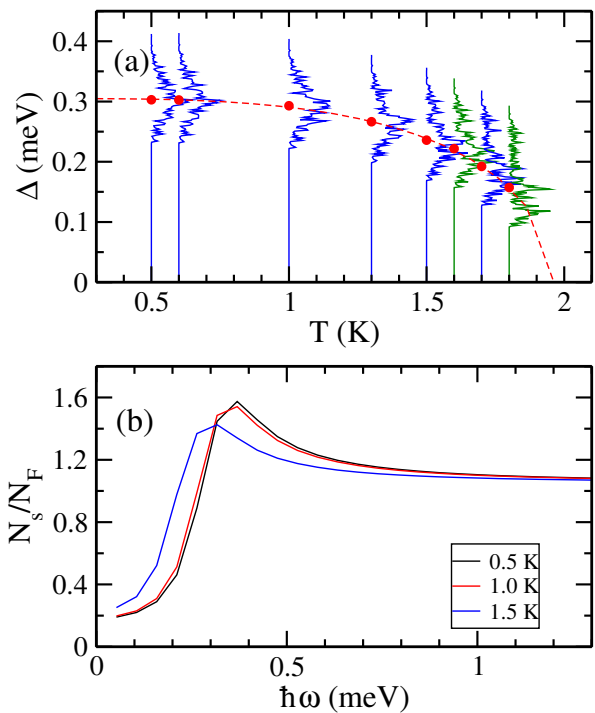


FIG. 8. (a) SC gap Δ as a function of temperature T , with the red dots denoting the averaged gap values, which are fitted using a BCS-type temperature dependence [Eq. (7)] (the dashed red curve). (b) Normalized SC quasiparticle DOS N_s/N_F as a function of energy calculated at several temperatures.

larger than 1.73 from the BCS theory, and this deviation from the universal BCS value may be attributed to the participation of multibands and SC gap anisotropy. With the knowledge of v_f (Fig. 4) and SC gap, the coherence length ξ can be estimated using the BCS relation $\xi = \hbar v_f / \pi \Delta$. The calculated average values of v_f and Δ are $\sim 1.2 \times 10^6$ m/s and ~ 0.305 meV, respectively, giving rise to ξ of $0.72 \mu\text{m}$. Interestingly, this ξ is about ten times larger than that of α -BiPd (66 nm) [32], and may be attributed to the higher Fermi velocity and lower SC gap magnitude in γ -BiPd.

Using Eq. (6), we also calculate the normalized quasiparticle DOS $\frac{N_s}{N_F}$ as a function of energy at several temperatures for γ -BiPd, as displayed in Fig. 8(b). Clearly, there is only one peak on the SC gap edge, indicating a single gap superconductivity in γ -BiPd. Furthermore, the $\frac{N_s}{N_F}$ spectrum shows a U-shaped function, further indicating a spin-singlet s -wave superconductivity in γ -BiPd (see, e.g., [64, 65]). This predicted $\frac{N_s}{N_F}$ spectra can be measured by using, e.g., scanning tunneling microscopy and spectroscopy (STM and STS) [69]. Indeed, this has recently been done for β -Bi₂Pd [65].

VIII. CONCLUSION

In summary, we have studied the SC properties of γ -BiPd by solving the anisotropic Migdal-Eliashberg equations in conjunction with *ab initio* relativistic calculations of the electron and phonon band structures as well as EPC matrix elements. We find that γ -BiPd possesses a complex FS, consisting of two electron pockets and one hole pocket, each characterised by distinct atomic orbitals. Importantly, we discover that the superconductivity in γ -BiPd is orbital-selective, arising from Bi *p*-orbitals, and distributed anisotropically on the FS. While our results show momentum \mathbf{k} -dependent EPC strength $\lambda_{\mathbf{k}}$ and SC gap $\Delta_{\mathbf{k}}$ across the FS, that calculated superconducting quasiparticle density of states N_S spectra exhibit a U-shaped gap and $\Delta_{\mathbf{k}}$ distribution forms a single peak, indicates a single gap spin-singlet *s*-wave superconductivity in this material. The calculated T_c is ~ 2.0 K, agreeing in order of magnitude with the experimental value of 3.3 K in γ -BiPd thin films [36]. Interestingly, the evaluated coherence length ξ of $0.72 \mu\text{m}$ is about ten times larger than that of α -BiPd (66 nm) [32]. The predicted EPC-enhanced Sommerfeld coefficient γ_n of $0.141 \text{ mJ/K}^2\text{cm}^3$ is close to the experimental γ_n value ($0.119 \text{ mJ/K}^2\text{cm}^3$) of the isoelectronic and isostructural Bi(Pd_{0.5}Pt_{0.5}) alloy [37]. Our interesting findings will stimulate further experiments on γ -BiPd, such as scanning tunneling microscopy and spectroscopy, quasiparticle interference imaging, high resolution angle-resolved photoemission spectroscopy and low temperature specific heat experiments.

ACKNOWLEDGMENTS

The authors acknowledge the support from the National Science and Technology Council (NSTC) and National Center for Theoretical Sciences (NCTS) in Taiwan. The authors also thank the National Center for High-performance Computing (NCHC) in Taiwan for the computing time.

APPENDIX A: Effect of Spin-Orbit Coupling on the Electronic Band Structure

Due to the presence of heavy Bi atoms in γ -BiPd, the relativistic SOC is expected to change the electronic band structure significantly. Thus, to examine the SOC effects, we have calculated the band structure of γ -BiPd both with and without including the SOC, and the results are shown in Fig. A1. It is clear from Fig. A1 that the presence of the SOC substantially alters the band structure, especially the energy bands near the E_F . In particular, the SOC opens a large gap of about 1.5 eV at the Dirac nodal point at ~ 1.4 eV above the E_F along the Γ -A symmetry line. This greatly pushes the lower band down to below the Fermi level, resulting in the disappearance of

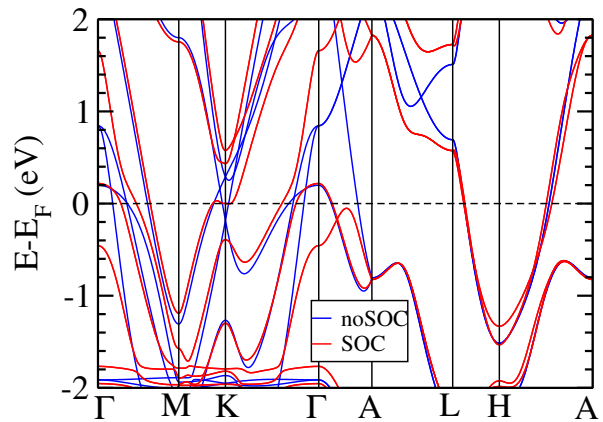


FIG. A1. Band structures of γ -BiPd calculated without (blue curves) and with (red curves) the SOC included.

the large hole pocket centered at the Γ point. Figure A1 also shows that the presence of the SOC greatly changes the band structure and FS topology near the K point in the vicinity of the E_F . Therefore, because of these significant effects of the SOC, we present only the results from the fully relativistic calculations in this paper.

APPENDIX B: Effect of Coulomb pseudopotential μ_c^* on SC gap function and T_c

The value of Coulomb pseudopotential μ_c^* would affect the calculated SC T_c and gap function $\Delta_{n\mathbf{k}}$. Generally, the larger μ_c^* value would result in the lower T_c and smaller $\Delta_{n\mathbf{k}}$. For a specific μ_c^* value, solving the anisotropic ME equations [Eqs. (1-2)] for $\Delta_{n\mathbf{k}}$ for many different temperatures to determine the T_c , is computationally extremely demanding, especially for the small SC gap cases [64] and also when T approaches to T_c . Thus, to examine the μ_c^* -dependence of T_c of γ -BiPd, we use the simplified Allen-Dynes McMillan (ADM) formula [59]

$$k_B T_c = \frac{\hbar\omega_{log}}{1.20} \exp\left[\frac{-1.04(1+\lambda)}{\lambda - \mu_c^*(1+0.62\lambda)}\right], \quad (\text{B1})$$

together with the calculated EPC constant λ and logarithmically averaged phonon frequency $\hbar\omega_{log}$ to estimate T_c , as listed in Table I. Nevertheless, we have also solved anisotropic ME equations [Eqs. (1-2)] at $T = 0.6$ K for four different μ_c^* values. The resultant SC gap functions

TABLE I. The average SC gap Δ_{avg} on the Fermi surface and transition temperature T_c for four different μ_c^* values. T_c is estimated using the ADM formula [Eq. (B1)] as well as the calculated EPC constant $\lambda = 0.46$ and $\hbar\omega_{log} = 8.3356$ meV.

μ_c^*	0.03	0.05	0.07	0.09
Δ_{avg}	0.373	0.303	0.243	0.193
T_c	2.196	1.738	1.331	0.980

$\Delta_{n\mathbf{k}}$ are displayed in Fig. A2 and the corresponding average gap Δ_{avg} values are listed in Table I.

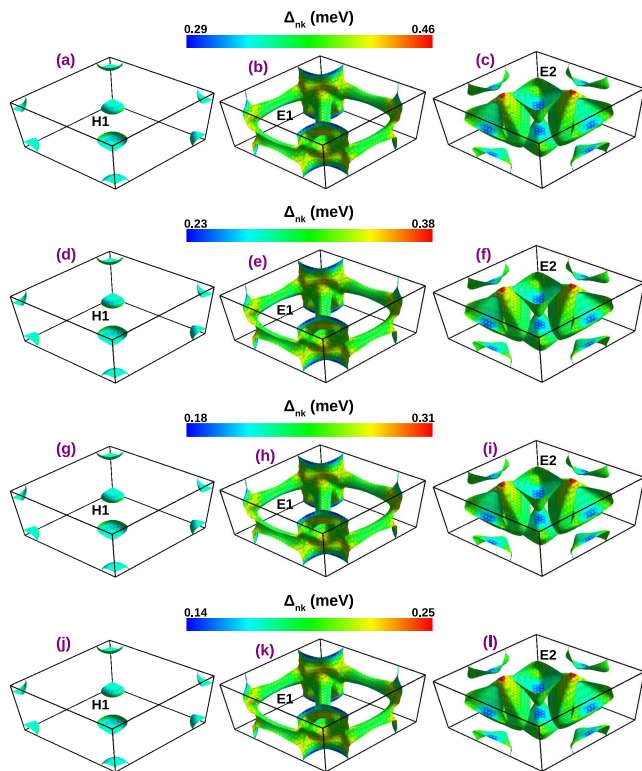


FIG. A2. Wave-vector \mathbf{k} -dependent SC gap function $\Delta_{n\mathbf{k}}$ at 0.6 K on the Fermi surface of γ -BiPd, calculated using μ_c^* of (a)–(c) 0.03, (d)–(f) 0.05, (g)–(i) 0.07, and (j)–(l) 0.09.

As expected, Table I shows that T_c decreases monotonically as μ_c^* increases. In particular, varying μ_c^* from 0.05 to 0.09 would reduce T_c by 0.76 K, from 2.20 K to 0.98 K. We note that T_c determined by solving the ME equations for the $\Delta_{n\mathbf{k}}$ as a function of T is slightly larger than that estimated using the ADM formula [Eq. (B1)]. For $\mu_c^* = 0.05$, T_c from the solutions of the ME equations is 1.96 K, being larger than that (1.74 K) from the ADM formula (see Table I). Figure A2 indicates that when the μ_c^* is altered, the pattern of SC gap function $\Delta_{n\mathbf{k}}$ hardly changes, although the magnitude of the SC gap decreases with increasing μ_c^* (see also Table I). Our choice of the lower μ_c^* value of 0.05 is based on the following two considerations. First, the theoretical T_c value (1.98 K) is in order of magnitude agreement with the experimental T_c value of ~ 3.40 K [36]. Second, the magnitude of the SC gap function $\Delta_{n\mathbf{k}}$ is sufficiently large so that stable solutions of the anisotropic ME equations could be numerically obtained within the available computing resources. The main subjects of the present paper are the anisotropic nature and orbital character of the SC gap function $\Delta_{n\mathbf{k}}$. Since the pattern of the calculated SC gap function $\Delta_{n\mathbf{k}}$ remains rather robust again a reasonable variation of μ_c^* used, the main conclusions made here are independent of the specific μ_c^* value used in this work. Of course, treating μ_c^* as a semiempirical parameter in the powerful ME theory is unsatisfactory. Indeed, fully *ab initio* ME theory in which the effective electron-electron Coulomb repulsion is determined from first-principles, has recently been developed [62]. Nevertheless, such fully *ab initio* ME theory calculations are beyond the scope of the present paper.

-
- [1] G. Binnig, A. Baratoff, H. E. Hoening, and J. G. Bednorz, Two-Band Superconductivity in Nb-Doped SrTiO₃, Phys. Rev. Lett. **45**, 1352 (1980).
- [2] H. Suhl, B. T. Matthias, and L. R. Walker, Bardeen-Cooper-Schrieffer Theory of Superconductivity in the Case of Overlapping Bands, Phys. Rev. Lett. **3**, 552 (1959).
- [3] J. Bardeen, L. N. Cooper, and J. R. Schrieffer, Theory of Superconductivity, Phys. Rev. **108**, 1175 (1957).
- [4] L. Komendova, Y. Chen, A. A. Shanenko, M. V. Milosevic, and F. M. Peeters, Two-Band Superconductors: Hidden Criticality Deep in the Superconducting State, Phys. Rev. Lett. **108**, 207002 (2012).
- [5] E. Babaev, Vortices with Fractional Flux in Two-Gap Superconductors and in Extended Faddeev Model, Phys. Rev. Lett. **89**, 067001 (2002).
- [6] J. Garaud, J. Carlstrom, and E. Babaev, Topological Solitons in Three-Band Superconductors with Broken Time Reversal Symmetry, Phys. Rev. Lett. **107**, 197001 (2011).
- [7] W. E. Pickett, Colloquium: Room temperature superconductivity: The roles of theory and materials design, Rev. Mod. Phys. **95**, 021001 (2023).
- [8] J. Nagamatsu, N. Nakagawa, T. Muranaka, Y. Zenitani, and J. Akimitsu, Superconductivity at 39 K in magnesium diboride, Nature **410**, 63 (2001).
- [9] D. G. Hinks, H. Claus, and J. D. Jorgensen, The complex nature of superconductivity in MgB₂ as revealed by the reduced total isotope effect, Nature **411**, 457 (2001).
- [10] F. Bouquet, R. A. Fisher, N. E. Phillips, D. G. Hinks, and J. D. Jorgensen, Specific Heat of MgB₂: Evidence for a Second Energy Gap, Phys. Rev. Lett. **97**, 047001 (2001).
- [11] M. Iavarone, G. Karapetrov, A. E. Koshelev, W. K. Kwok, G. W. Crabtree, D. G. Hinks, W. N. Kang, E.-M. Choi, H. J. Kim, H.-J. Kim, and S. I. Lee, Two-Band Superconductivity in MgB₂, Phys. Rev. Lett. **89**, 187002 (2002).
- [12] S. Souma, Y. Machida, T. Sato, T. Takahashi, H. Matsui, S.-C. Wang, H. Ding, A. Kaminski, J. Campuzano, S. Sasaki, *et al.*, The origin of multiple superconducting gaps in MgB₂, Nature **423**, 65 (2003).
- [13] P. O. Sprau, A. Kostin, A. Kreisel, A. E. Böhrer, V. Tau-four, P. C. Canfield, S. Mukherjee, P. J. Hirschfeld, B. M. Andersen, and J. S. Davis, Discovery of orbital-selective Cooper pairing in FeSe, Science **357**, 75 (2017).
- [14] E. M. Nica, R. Yu, and Q. Si, Orbital-selective pairing and superconductivity in iron selenides, npj Quantum

- Materials **2**, 24 (2017).
- [15] A. Kreisel, B. M. Andersen, P. O. Sprau, A. Kostin, J. C. S. Davis, and P. J. Hirschfeld, Orbital selective pairing and gap structures of iron-based superconductors, *Phys. Rev. B* **95**, 174504 (2017).
- [16] A. Kostin, P. O. Sprau, A. Kreisel, Y. X. Chong, A. E. Böhmer, P. C. Canfield, P. J. Hirschfeld, B. M. Andersen, and J. S. Davis, Imaging orbital-selective quasiparticles in the Hund's metal state of FeSe, *Nature Materials* **17**, 869 (2018).
- [17] H. Hu, R. Yu, E. M. Nica, J.-X. Zhu, and Q. Si, Orbital-selective superconductivity in the nematic phase of FeSe, *Phys. Rev. B* **98**, 220503 (2018).
- [18] K. Kuroki, S. Onari, R. Arita, H. Usui, Y. Tanaka, H. Kontani, and H. Aoki, Unconventional Pairing Originating from the Disconnected Fermi Surfaces of Superconducting LaFeAsO_{1-x}F_x, *Phys. Rev. Lett.* **101**, 087004 (2008).
- [19] I. I. Mazin, D. J. Singh, M. D. Johannes, and M. H. Du, Unconventional Superconductivity with a Sign Reversal in the Order Parameter of LaFeAsO_{1-x}F_x, *Phys. Rev. Lett.* **101**, 057003 (2008).
- [20] X. Dai, Z. Fang, Y. Zhou, and F.-C. Zhang, Even Parity, Orbital Singlet, and Spin Triplet Pairing for Superconducting LaFeAsO_{1-x}F_x, *Phys. Rev. Lett.* **101**, 057008 (2008).
- [21] M. Yi, Y. Zhang, Z.-X. Shen, and D. Lu, Role of the orbital degree of freedom in iron-based superconductors, *npj Quantum Materials* **2**, 57 (2017).
- [22] E. M. Nica and Q. Si, Multiorbital singlet pairing and d+d superconductivity, *npj Quantum Materials* **6**, 3 (2021).
- [23] C. Heil, S. Poncé, H. Lambert, M. Schlipf, E. R. Margine, and F. Giustino, Origin of Superconductivity and Latent Charge Density Wave in NbS₂, *Phys. Rev. Lett.* **119**, 087003 (2017).
- [24] X. Bi, Z. Li, J. Huang, F. Qin, C. Zhang, Z. Xu, L. Zhou, M. Tang, C. Qiu, P. Tang, T. Ideue, T. Nojima, Y. Iwasa, and H. Yuan, Orbital-selective two-dimensional superconductivity in NbS₂, *Phys. Rev. Res.* **4**, 013188 (2022).
- [25] I. Guillamon, H. Suderow, S. Vieira, L. Cario, P. Diener, and P. Rodiere, Superconducting Density of States and Vortex Cores of 2H – NbS₂, *Phys. Rev. Lett.* **101**, 166407 (2008).
- [26] T. Yokoya, T. Kiss, A. Chainani, S. Shin, M. Nohara, and H. Takagi, Fermi surface sheet-dependent superconductivity in 2H – NbSe₂, *Science* **294**, 2518 (2001).
- [27] T. Antonelli, W. Rahim, M. D. Watson, A. Rajan, O. J. Clark, A. Danilenko, K. Underwood, I. Marković, E. Abarca-Morales, S. R. Kavanagh, *et al.*, Orbital-selective band hybridisation at the charge density wave transition in monolayer TiTe₂, *npj Quantum Materials* **7**, 98 (2022).
- [28] F. Tafti, A. Juneau-Fecteau, M.-E. Delage, S. René de Cotret, J.-P. Reid, A. Wang, X. Luo, X. Chen, N. Doiron-Leyraud, and L. Taillefer, Sudden reversal in the pressure dependence of T_c in the iron-based superconductor KFe₂As₂, *Nature Physics* **9**, 349 (2013).
- [29] B. Joshi, A. Thamizhavel, and S. Ramakrishnan, Superconductivity in noncentrosymmetric BiPd, *Phys. Rev. B* **84**, 064518 (2011).
- [30] Y. Imai, F. Nabeshima, T. Yoshinaka, K. Miyatani, R. Kondo, S. Komiya, I. Tsukada, and A. Maeda, Superconductivity at 5.4 K in β -Bi₂Pd, *J. Phys. Soc. Jpn.* **81**, 113708 (2012).
- [31] M. Sakano, K. Okawa, M. Kanou, H. Sanjo, T. Okuda, T. Sasagawa, and K. Ishizaka, Topologically protected surface states in a centrosymmetric superconductor β -PdBi₂, *Nature Communications* **6**, 8595 (2015).
- [32] Z. Sun, M. Enayat, A. Maldonado, C. Lithgow, E. Yelland, D. C. Peets, A. Yaresko, A. P. Schnyder, and P. Wahl, Dirac surface states and nature of superconductivity in noncentrosymmetric BiPd, *Nature Communications* **6**, 6633 (2015).
- [33] K. Iwaya, Y. Kohsaka, K. Okawa, T. Machida, M. Bahramy, T. Hanaguri, and T. Sasagawa, Full-gap superconductivity in spin-polarised surface states of topological semimetal β -PdBi₂, *Nature Communications* **8**, 976 (2017).
- [34] J. Kacmarcik, Z. Pribulova, T. Samuely, P. Szabo, V. Cambel, J. Soltys, E. Herrera, H. Suderow, A. Correa Orellana, D. Prabhakaran, and P. Samuely, Single-gap superconductivity in β -Bi₂Pd, *Phys. Rev. B* **93**, 144502 (2016).
- [35] S. Mitra, K. Okawa, S. Kunniniyil Sudheesh, T. Sasagawa, Jian Xin Zhu, Elbert E. M. Chia, Probing the superconducting gap symmetry of α -PdBi₂: A penetration depth study, *Phys. Rev. B* **95**, 134519 (2017).
- [36] C. C. Chiang, H. C. Lee, S. C. Lin, D. Qu, M. W. Chu, C. D. Chen, C. L. Chien, and S. Y. Huang, Unequivocal Identification of Spin-Triplet and Spin-Singlet Superconductors with Upper Critical Field and Flux Quantization, *Phys. Rev. Lett.* **131**, 236003 (2023).
- [37] S. Sharma, A. D. S. Richards, K. P. Sajilesh, A. Kataria, B. S. Agboola, M. Pula, J. Gautreau, A. Ghara, D. Singh, S. Mark *et al.*, Evidence for conventional superconductivity in Bi₂PdPt and prediction of possible topological superconductivity in disorder-free γ -BiPd, *Phys. Rev. B* **109**, 224509 (2024).
- [38] M. Heise, J.-H. Chang, R. Schonemann, T. Herrmannsdorfer, J. Wosnitza, and M. Ruck, Full access to nanoscale bismuth-palladium intermetallics by low-temperature syntheses, *Chemistry of Materials* **26**, 5640 (2014).
- [39] X. Xu, Y. Li, and C. L. Chien, Spin-Triplet Pairing State Evidenced by Half-Quantum Flux in a Noncentrosymmetric Superconductor, *Phys. Rev. Lett.* **124**, 167001 (2020).
- [40] M. Sigrist, D. Agterberg, P. Frigeri, N. Hayashi, R. Kaur, A. Koga, I. Milat, K. Wakabayashi, and Y. Yanase, Superconductivity in non-centrosymmetric materials, *Journal of Magnetism and Magnetic Materials* **310**, 536 (2007).
- [41] F. Kneidinger, E. Bauer, I. Zeiringer, P. Rogl, C. Blaas Schenner, D. Reith, and R. Podloucky, Superconductivity in non-centrosymmetric materials, *Physica C: Superconductivity and its Applications* **514**, 388 (2015).
- [42] S. Thirupathiah, S. Ghosh, R. Jha, E. D. L. Rienks, K. Dolui, V. V. Ravi Kishore, B. Buchner, T. Das, V. P. S. Awana, D. D. Sarma, and J. Fink, Unusual Dirac Fermions on the Surface of a Noncentrosymmetric α -BiPd Superconductor, *Phys. Rev. Lett.* **117**, 177001 (2016).
- [43] F. Lupke, D. Waters, S. C. de la Barrera, M. Widom, D. G. Mandrus, J. Yan, R. M. Feenstra, and B. M. Hunt, Proximity-induced superconducting gap in the quantum spin Hall edge state of monolayer WTe₂, *Nature Physics* **16**, 526 (2020).
- [44] M. Ben Shalom, M. Sachs, D. Rakhmilevitch, A.

- Palevski, and Y. Dagan, Tuning Spin-Orbit Coupling and Superconductivity at the SrTiO₃/LaAlO₃ Interface: A Magnetotransport Study, *Phys. Rev. Lett.* **104**, 126802 (2010).
- [45] A. D. Caviglia, M. Gabay, S. Gariglio, N. Reyren, C. Cancellieri, and J. M. Triscone, Tunable Rashba spin-orbit interaction at oxide interfaces, *Tunable Rashba Spin-Orbit Interaction at Oxide Interfaces*, *Phys. Rev. Lett.* **104**, 126803 (2010).
- [46] D. A. Dikin, M. Mehta, C. W. Bark, C. M. Folkman, C. B. Eom, and V. Chandrasekhar, Coexistence of Superconductivity and Ferromagnetism in Two Dimensions, *Phys. Rev. Lett.* **107**, 056802 (2011).
- [47] K. Michaeli, A. C. Potter, and P. A. Lee, Superconducting and Ferromagnetic Phases in SrTiO₃/LaAlO₃ Oxide Interface Structures: Possibility of Finite Momentum Pairing, *Phys. Rev. Lett.* **108**, 117003 (2012).
- [48] M. Flokstra, R. Stewart, C. M. Yim, C. Trainer, P. Wahl, D. Miller, N. Satchell, G. Burnell, H. Luetkens, T. Prokscha, *et al.*, Spin-orbit driven superconducting proximity effects in Pt/Nb thin films, *Nature Communications* **14**, 5081 (2023).
- [49] Y. Saito, Y. Nakamura, M. S. Bahramy, Y. Kohama, J. Ye, Y. Kasahara, Y. Nakagawa, M. Onga, M. Tokunaga, T. Nojima, *et al.*, Superconductivity protected by spin-valley locking in ion-gated MoS₂, *Nature Physics* **12**, 144 (2016).
- [50] J. Lu, O. Zheliuk, I. Leermakers, N. F. Yuan, U. Zeitler, K. T. Law, and J. Ye, Evidence for two-dimensional Ising superconductivity in gated MoS₂, *Science* **350**, 1353 (2015).
- [51] X. Xi, Z. Wang, W. Zhao, J. H. Park, K. T. Law, H. Berger, L. Forro, J. Shan, and K. F. Mak, Ising pairing in superconducting NbSe₂ atomic layers, *Nature Physics* **12**, 139 (2016).
- [52] J. Falson, Y. Xu, M. Liao, Y. Zang, K. Zhu, C. Wang, Z. Zhang, H. Liu, W. Duan, K. He, *et al.*, Type-II Ising pairing in few-layer stanene, *Science* **367**, 1454 (2020).
- [53] E. R. Margine and F. Giustino, Anisotropic Migdal-Eliashberg theory using Wannier functions, *Phys. Rev. B* **87**, 024505 (2013).
- [54] P. Giannozzi, S. Baroni, N. Bonini, M. Calandra, R. Car, C. Cavazzoni, D. Ceresoli, G. L. Chiarotti, M. Cococcioni, I. Dabo, *et al.*, QUANTUM ESPRESSO: a modular and open-source software project for quantum simulations of materials, *Journal of Physics: Condensed Matter* **21**, 395502 (2009).
- [55] P. Giannozzi, O. Andreussi, T. Brumme, O. Bunau, M. B. Nardelli, M. Calandra, R. Car, C. Cavazzoni, D. Ceresoli, M. Cococcioni, *et al.*, Advanced capabilities for materials modelling with Quantum ESPRESSO, *Journal of Physics: Condensed Matter* **29**, 465901 (2017).
- [56] D. R. Hamann, Optimized norm-conserving Vanderbilt pseudopotentials, *Phys. Rev. B* **88**, 085117 (2013).
- [57] S. Baroni, S. de Gironcoli, A. Dal Corso, and P. Giannozzi, Phonons and related crystal properties from density-functional perturbation theory, *Rev. Mod. Phys.* **73**, 515 (2001).
- [58] S. Ponce, E. R. Margine, C. Verdi, and F. Giustino, EPW: Electron-phonon coupling, transport and superconducting properties using maximally localized Wannier functions, *Computer Physics Communications* **209**, 116 (2016).
- [59] H. Lee, S. Ponce, K. Bushick, S. Hajinazar, J. Lafuente Bartolome, J. Leveillee, C. Lian, J. M. Lihm, F. Macheda, H. Mori, *et al.*, Electron-phonon physics from first principles using the EPW code, *npj Computational Materials* **9**, 156 (2023).
- [60] J. Noffsinger, F. Giustino, B. D. Malone, C.-H. Park, S. G. Louie, and M. L. Cohen, EPW: A program for calculating the electron-phonon coupling using maximally localized Wannier functions, *Computer Physics Communications* **181**, 2140 (2010).
- [61] P. Bayliss, The American Mineralogist Crystal Structure Database <http://ruff.geo.arizona.edu/AMS/amcsd.php>.
- [62] C. Pellegrini, R. Heid, A. Sanna, Eliashberg theory with ab-initio Coulomb interactions: a minimal numerical scheme applied to layered superconductors, *J. Phys. Mater.* **5** 024007 (2022).
- [63] W. L. McMillan, Transition Temperature of Strong-Coupled Superconductors, *Phys. Rev.* **167**, 331 (1968).
- [64] Z. Li and S. G. Louie, Two-Gap Superconductivity and the Decisive Role of Rare-Earth *d* Electrons in Infinite-Layer Nickelates, *Phys. Rev. Lett.* **133**, 126401 (2024).
- [65] E. Herrera, I. Guillamon, J. A. Galvis, A. Corra, A. Fente, R. F. Lucas, F. J. Mompean, M. Garcia-Hernandez, S. Vierira, J. P. and H. Suderow, Magnetic field dependence of the density of states in the multiband superconductor β -Bi₂Pd, *Phys. Rev. B* **92**, 054507 (2015).
- [66] C.-S. Lian, C. Si and W. Duan, Single anisotropic gap superconductivity and proximity effect in PbTaSe₂, *Phys. Rev. B* **100**, 235420 (2019).
- [67] A. Damascelli, Z. Hussain, and Z. X. Shen, Angle-resolved photoemission studies of the cuprate superconductors, *Rev. Mod. Phys.* **75**, 473 (2003).
- [68] D. Mou, S. Liu, X. Jia, J. He, Y. Peng, L. Zhao, L. Yu, G. Liu, S. He, X. Dong *et al.*, Distinct Fermi Surface Topology and Nodeless Superconducting Gap in a Tl_{0.58}Rb_{0.42}Fe_{1.72}Se₂ Superconductor, *Phys. Rev. Lett.* **106**, 107001 (2011).
- [69] O. Fischer, M. Kugler, I. Maggio Aprile, C. Berthod, and C. Renner, Scanning tunneling spectroscopy of high-temperature superconductors, *Rev. Mod. Phys.* **79**, 353 (2007).